A Simple Analytical Model of the Diurnal Ekman Layer

JACOB O. WENEGRAT[a]

Joint Institute for the Study of the Atmosphere and Ocean, University of Washington, Seattle, Washington

MICHAEL J. MCPHADEN

NOAA/Pacific Marine Environmental Laboratory, Seattle, Washington

(Manuscript received 27 January 2016, in final form 7 July 2016)

ABSTRACT

The effects of time-varying turbulent viscosity on horizontal currents in the ocean surface boundary layer are considered using a simple, theoretical model that can be solved analytically. This model reproduces major aspects of the near-surface ocean diurnal cycle in velocity and shear, while retaining direct parallels to the steady-state Ekman solution. The parameter dependence of the solution is explored, and quantitative measures of the low-frequency rectification of velocity and shear are derived. Results demonstrate that time variability in eddy viscosity leads to significant changes to the time-averaged velocity and shear fields, with important implications for the interpretation of observations and modeling of the near-surface ocean. These findings mirror those of more complete numerical modeling studies, suggesting that some of the rectification mechanisms active in those studies may be independent of the details of the boundary layer turbulence.

1. Introduction

The daily transit of the sun causes a daily cycle in surface heat flux that is a principal forcing of upper-ocean variability. This diurnal cycle in surface heat flux leads to a diurnal cycle in temperature, stratification, and near-surface mixing (Smyth 1854; Stommel et al. 1969; Brainerd and Gregg 1993). The effects of these changes have been the subject of widespread study in the oceanographic literature, and beyond the purely physical implications, a host of biophysical interactions on the diurnal scale have been identified (McCreary et al. 2001; Kawai and Wada 2007). The effects of the ocean diurnal cycle have also been studied extensively from the atmospheric perspective, as diurnal sea surface temperature variability is critical to atmospheric boundary layer moisture content and convection, which respond nonlinearly to temperature (Chen and Houze 1997; Clayson and Chen 2002; Dai and Trenberth 2004). The ability of the diurnal cycle in surface heat flux to modify low-frequency ocean temperature variability, a process termed rectification, has also been studied in the context of models, where it is shown that diurnal variability modifies the mean state on intraseasonal and longer time scales (Shinoda 2005; Danabasoglu et al. 2006; Bernie et al. 2007, 2008).

While the ocean thermodynamic response to diurnal time-scale forcing has been the subject of extensive work, the dynamic response remains less well understood. Observations have established that diurnal variability in stratification can serve to inhibit turbulent vertical momentum flux, causing the near-surface convergence of wind-driven momentum that leads to the acceleration of a downwind diurnal jet (Price et al. 1986). These jets are highly sheared, lowering the flow Richardson number to allow for the development of shear instabilities that deepen the mixed layer before the surface heat flux has changed sign, suggesting the dynamics of the ocean response are intertwined with the thermodynamic response (Smyth et al. 2013; Wenegrat and McPhaden 2015). Diurnal variability of mixing has also been implicated in

---

[a] Current affiliation: Department of Environmental Earth System Science, Stanford University, Stanford, California.

Joint Institute for the Study of the Atmosphere and Ocean Contribution Number 2495 and Pacific Marine Environmental Laboratory Contribution Number 4418.

Corresponding author address: Jacob O. Wenegrat, Department of Environmental Earth System Science, Stanford University, 473 Via Ortega, Stanford, CA 94305.
E-mail: jwenegrat@stanford.edu

DOI: 10.1175/JPO-D-16-0031.1

departures of time-averaged velocity fields from the predictions of classic Ekman theory (Price and Sundermeyer 1999), although the observational evidence alone has not been conclusive in this regards (Lewis and Belcher 2004; Rascle and Ardhuin 2009).

Much of the theoretical work on the dynamics of the ocean diurnal cycle has focused on the use of slab layer models, which, while useful in their simplicity, by construction do not offer any insight into the vertical structure of the flow. Further, observations suggest that Ekman theory provides a more consistent description of subinertial variability than slab layer models do (Davis et al. 1981; Weller and Plueddemann 1996; Elipot and Gille 2009; Kim et al. 2014), and hence utilizing slab layer physics to understand rectification effects may not be appropriate. Thus, despite the recognized importance of the diurnal cycle, questions remain about the dynamical response to diurnal forcing, in particular regarding the possible routes to dynamical rectification.

Important work on this topic was undertaken by McWilliams and Huckle (2006), and McWilliams et al. (2009), in the context of idealized numerical models. They showed that transient winds, surface buoyancy fluxes, and interior eddy fluxes result in rectification to the time-mean flow, attributed principally to modifications of the turbulent boundary layer depth and nonlinearities in the parameterized eddy viscosity (McWilliams and Huckle 2006; McWilliams et al. 2009). These findings are significant contributions to our understanding of dynamical rectification effects, particularly in their ability to elucidate the terms controlling changes in turbulent mixing under different forcing regimes. However, as is often the case, the greater physical realism enabled by a numerical model comes at the expense of additional complexity, and thus the parameter dependence and underlying physics are not as clearly illuminated as with theoretical approaches.

Here, we take a simpler approach, situated in complexity between analytic slab layer models and more realistic numerical models, and consider a periodic solution for the time-dependent Ekman layer (section 2). The eddy viscosity is treated as an external parameter, allowed to vary sinusoidally in time to approximate the known time variability of turbulent mixing. This approach excludes any feedbacks between the wind-driven shear and the eddy viscosity, which is at best a crude, first-order approximation (cf. McWilliams et al. 2009). However, the ability of the resulting model to reproduce major aspects of the diurnal cycle in the near-surface ocean, as well its analytic tractability and possibility for insight into the underlying physical processes, particularly dynamical rectification, are advantageous (section 3). In this respect, aspects of this work are similar to approaches used extensively in the study of the dynamics of low-level jets in the atmospheric boundary layer (Buajitti and Blackadar 1957; Singh et al. 1993; Tan and Farahani 1998; Zhang and Tan 2002), which to our knowledge have not yet been applied to the oceanographic problem.

2. Theory

We consider a linearized model of time-dependent horizontal flow, written using complex notation as $\mathbf{u} = u + iv$. The horizontal momentum equations are thus given by

$$\mathbf{u}_t + if\mathbf{u} = -\frac{1}{\rho}\nabla p + [A_\nu(z,t)\mathbf{u}_z]_z, \tag{1}$$

with subscripts t and z denoting differentiation with respect to time and the vertical coordinate, respectively. The eddy viscosity is denoted as A_ν, f is the Coriolis frequency, and the density is denoted by ρ. It is assumed that the horizontal pressure gradient ∇p is independent of z, allowing separation into geostrophic and ageostrophic components, although we caution that baroclinic pressure gradients can be expected to significantly modify ageostrophic flows in the real ocean (Wenegrat and McPhaden 2016). The focus of this work is on the wind-driven flow; hence, for the remainder we set $\nabla p = 0$. We thus seek a solution to

$$\mathbf{u}_t + if\mathbf{u} = [A_\nu(z,t)\mathbf{u}_z]_z. \tag{2}$$

Transforming $\mathbf{u} = e^{-ift}\mathbf{w}$ reduces (2) to the one-dimensional heat equation with a coefficient that varies in both time and space:

$$\mathbf{w}_t = [A_\nu(z,t)\mathbf{w}_z]_z. \tag{3}$$

Similar equations arise in the study of a variety of physical phenomenon, including non-Newtonian fluids (Balmforth and Craster 2001), diffusion in porous materials such as concrete (Mangat and Molloy 1994), and heat conduction in radioactive materials (Cannon 1984). For vertically uniform A_ν, with arbitrary time dependence, it is possible to find a unique transformation of the time coordinate such that the solution can be written as a convolution between a transfer function and the time-varying surface wind stress (cf. Cannon 1984, 13.1.1–13.1.8). An example integral solution for an impulsively started steady wind stress $\boldsymbol{\tau}$ was given by Csanady and Shaw (1980):

$$\mathbf{u}(z,t) = \frac{\boldsymbol{\tau}}{\rho}\int_0^t \frac{e^{-if(t-\eta)}}{\sqrt{\pi Q(\eta)}} e^{-\{z^2/[4Q(\eta)]\}}\, d\eta, \quad \text{and} \tag{4}$$

$$Q(y) = \int_{t-y}^{t} A_\nu(T)\,dT. \tag{5}$$

This solution was extended to time-varying wind stress in Wenegrat (2016), where it was found that monochromatic, periodic time variability in A_ν introduces a complex modulation of the ocean velocity field at all frequencies. Here, we take advantage of the existence of an oscillatory steady-state solution for the case of steady wind stress that was evident in this earlier work (Wenegrat 2016) to provide a simple time periodic solution for the case of steady wind forcing and periodically varying $A_\nu(z, t)$.

We thus seek solutions of (2), subject to the following conditions:

$$\mathbf{u}(z,t) = \mathbf{u}\left(z, t + \frac{2\pi}{\omega}\right), \tag{6a}$$

$$\mathbf{u}_z(0,t) = \frac{\boldsymbol{\tau}_w}{\rho A_\nu(0,t)}, \quad \text{and} \tag{6b}$$

$$\mathbf{u} \to 0, z \to -\infty. \tag{6c}$$

Equation (6a) expresses the periodic time boundary condition, with frequency ω. For the motivating reasons given in section 1, we will identify this with the diurnal frequency, although the solution is valid generally for any ω. The surface boundary condition (6b) is the standard shear stress boundary condition where the wind stress is assumed constant in time, and the eddy viscosity is allowed to be a function of both time and space $A_\nu(z, t)$. The results discussed here are not sensitive to the particular bottom boundary condition, hence, for simplicity we use (6c), the standard Ekman bottom boundary condition. The derivation given can easily be applied to alternate boundary conditions.

The eddy viscosity $A_\nu(z, t)$ is assumed to be a known parameter, and we require that it be separable in time and space: $A_\nu(z, t) = A(z)K(t)$. The dimensional vertical structure $A(z)$ can take any form that satisfies the requirements of a Wentzel–Kramers–Brillouin–Jeffreys approximation (WKBJ; Bender and Orszag 1978), which is discussed below. However, we require that the time dependence take a particular form (Buajitti and Blackadar 1957)

$$K(t) = 1 + \delta\, cos(\omega t), \tag{7}$$

with $\delta \in [0, 1)$, determining the strength of the periodic cycle of mixing. These mathematically expedient requirements on A_ν are not expected to accurately reflect the diurnal cycle of near-surface mixing, which remains an active area of observational work. Notably, parameterizations based on similarity theory with a time-varying boundary layer depth, such as the K-profile parameterization (KPP; Large et al. 1994), result in A_ν, where space–time dependence is not formally separable, discussed further in appendix A.

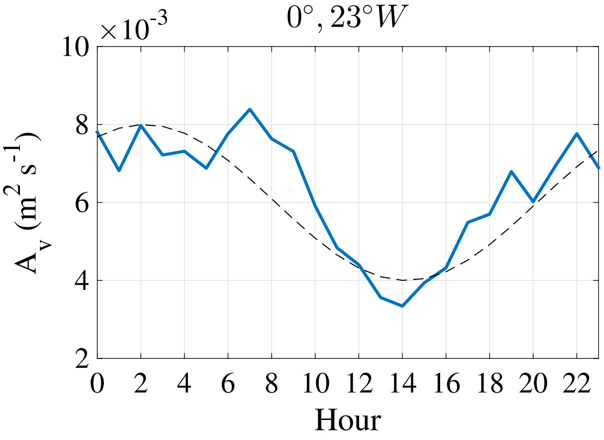

FIG. 1. Composite diurnal cycle in A_ν at 0°, 23°W, $z = -5.6$ m, inferred from observations (blue) from 13 Oct 2008 through 6 Jan 2009, as discussed in Wenegrat and McPhaden (2015, their section 4.1). Also shown is a sinusoidal approximation to the composite diurnal cycle (dashed, with $A_{\nu_0} = 6 \times 10^{-3}\,\mathrm{m^2\,s^{-1}}$ and $\delta = 0.3$).

However, the idealized form of A_ν that we use here can be justified in part based on observations of the diurnal cycle of near-surface A_ν, which suggests that a sinusoidal time dependence is a reasonable first approximation (Wenegrat and McPhaden 2015). An example composite diurnal cycle, estimated indirectly from ~3 months of moored observations of wind stress and near-surface velocity, following the method given in Wenegrat et al. (2014), is shown in Fig. 1, demonstrating the essentially sinusoidal time dependence. Further support for this idealized time dependence of A_ν comes from a posteriori comparisons of the theory with more complete numerical models (section 3a, and appendix A). Note also that the periodic time variability in (7) introduces no change to the diurnally averaged A_ν, which facilitates comparison to the steady ($\delta = 0$) solution.

We can rewrite (3) as

$$\mathbf{w}_t(z,t) = K(t)[A(z)\mathbf{w}(z,t)_z]_z. \tag{8}$$

Transforming the time coordinate, such that $\zeta = t + \delta/\omega \sin(\omega t)$, gives

$$\mathbf{w}_\zeta = [A(z)\mathbf{w}_z]_z. \tag{9}$$

In the new coordinate system, the time periodic condition (6a) can be written as $\mathbf{w}[z, \zeta + (2\pi/\omega)] = \mathbf{w}(z, \zeta)e^{if(2\pi/\omega)}$ (Zhang and Tan 2002), which is true of

$$\mathbf{w}(z,\zeta) = \mathbf{W}\sum_{n=-\infty}^{\infty}\mathbf{w}_n(z)e^{i(f+n\omega)\zeta}, \qquad (10)$$

where $\mathbf{W}$ is a complex constant. Substituting (10) into (9) gives a series of ordinary differential equations:

$$[A(z)(\mathbf{w}_n)_z]_z - i(f+n\omega)\mathbf{w}_n = 0, \qquad (11)$$

which are equivalent to those studied by Zhang and Tan (2002).

Each of the n equations defined by (11) are straightforward to solve numerically, or, for additional insight into the dynamics, the solutions can be approximated using the WKBJ method (Grisogono 1995), which assumes

$$w_n \propto e^{(1/\varepsilon_n)(S_0+\varepsilon_n S_1+\varepsilon_n^2 S_2\cdots)}. \qquad (12)$$

Nondimensionalizing in the standard manner for the Ekman balance (e.g., Vallis 2006, section 2.12.1) with a modified rotational frequency of $f + n\omega$ gives

$$\mathrm{Ek}_n[\hat{A}(z)(\hat{w}_n)_{\hat{z}\hat{z}} + \hat{A}(z)_{\hat{z}}\hat{w}_{\hat{z}}] - i\hat{w} = 0, \qquad (13)$$

where the hat notation indicates nondimensional quantities, $\mathrm{Ek}_n = A_0/[(f+n\omega)D^2]$ is the mode Ekman number, and A_0 is a representative-scale value of A_ν. We identify D with the depth scale over which $A(z)$ varies, as per the discussion in Wenegrat and McPhaden (2016); Ek_n thus characterizes the ratio of the depth scale of the nth mode boundary layer to the depth scale over which $A(z)$ varies. Using (12) in (13) gives $\varepsilon_n \sim \mathrm{Ek}_n^{1/2}$ and the WKBJ balance equations:

$$S_0 = \sqrt{i}\int_z^0 \hat{A}(Z)^{-1/2}\,dZ, \quad \text{and} \qquad (14)$$

$$S_1 = -\frac{1}{4}\log\hat{A}(z). \qquad (15)$$

Use of the WKBJ approximation requires that

$$\frac{\mathrm{Ek}_n^{1/2}S_1}{S_0} \ll 1, \quad \mathrm{Ek}_n^{1/2} \to 0, \qquad (16)$$

$$\mathrm{Ek}_n^{1/2}S_2 \ll 1, \quad \mathrm{Ek}_n^{1/2} \to 0, \qquad (17)$$

which physically can be understood as requiring slow variation of A_ν relative to the boundary layer thickness of the nth mode. The constraint this places on the validity of the WKBJ approximation will be strongest for the $n = 0$ mode, as higher modes become rapidly surface trapped. A specific case where this WKBJ expansion is formally incorrect is the case of $f = \pm n\omega$, where mode $\mp n$ will have $\mathrm{Ek}_n \to \infty$. However, these modes are zeros of the Bessel functions used in the solutions below and so do not contribute appreciably to the total solution; this is discussed in more detail in appendix B.

To simplify the analysis, we consider only simple profiles of $A(z)$ that stay sufficiently large so as to not violate (16), which precludes the direct application of this approximation to many common forms of parameterized A_ν (O'Brien 1970; Large et al. 1994). If desired, this requirement can be removed by patching an appropriate inner solution as in Wenegrat and McPhaden (2016). However, as discussed below, many of the results emphasized here are independent of the particular form of $A(z)$.

The solution for an arbitrary mode after application of the bottom boundary condition is thus

$$\mathbf{w}_n(z) = C_n A(z)^{-1/4}e^{-(1+i)\int_z^0 h_{\mathrm{Ek}_n}^{-1}(Z)dZ}, \qquad (18)$$

such that h_{Ek_n} defines the mode's depth-dependent Ekman depth: $h_{\mathrm{Ek}_n}(z) = \sqrt{2A(z)/(f+n\omega)}$.

The surface boundary condition (6b) can be considered by returning to the series expansion (10) in terms of $w_z(z, \zeta)$:

$$\sum_{n=-\infty}^{\infty} C_n\frac{\sqrt{2i}\chi_n(0)h_{\mathrm{Ek}_0}(0)}{A(0)^{1/4}h_{\mathrm{Ek}_n}(0)}e^{[i(f+n\omega)\zeta]} = \frac{e^{ift(\zeta)}}{K[t(\zeta)]}, \qquad (19)$$

where we have set $\mathbf{W} = \boldsymbol{\tau}_w h_{\mathrm{Ek}_0}(0)[A(0)\rho]^{-1}$ and

$$\chi_n(z) = 1 - \frac{\sqrt{-2i}}{8}\frac{A(z)_z}{A(z)}h_{\mathrm{Ek}_n}(z). \qquad (20)$$

Transforming back to the original time coordinate, writing (7) as $K(t) = 1 + \delta/2(e^{i\omega t} + e^{-i\omega t})$, and dividing (19) through by the right-hand side gives

$$\sum_{n=-\infty}^{\infty} C_n\frac{\sqrt{2i}\chi_n(0)h_{\mathrm{Ek}_0}(0)}{A(0)^{1/4}h_{\mathrm{Ek}_n}(0)}\left\{e^{in\omega t+i\delta[(f/\omega)+n]sin(\omega t)} + \frac{\delta}{2}e^{i(n+1)\omega t+i\delta[(f/\omega)+n]sin(\omega t)} + \frac{\delta}{2}e^{i(n-1)\omega t+i\delta[(f/\omega)+n]sin(\omega t)}\right\} = 1. \qquad (21)$$

Note that if integrated in time each of the exponential terms takes the form of a Bessel function of the first kind (Temme 1996; Zhang and Tan 2002); thus,

$$\sum_{n=-\infty}^{\infty}(-1)^n C_n \frac{\sqrt{2i}\chi_n(0)h_{\mathrm{Ek}_0}(0)}{A(0)^{1/4}h_{\mathrm{Ek}_n}(0)}\left\{J_n\left[\delta\left(\frac{f}{\omega}+n\right)\right]-\frac{\delta}{2}J_{n+1}\left[\delta\left(\frac{f}{\omega}+n\right)\right]-\frac{\delta}{2}J_{n-1}\left[\delta\left(\frac{f}{\omega}+n\right)\right]\right\}=1, \tag{22}$$

where J_n denotes the nth Bessel function of the first kind (Temme 1996). The surface boundary condition is therefore satisfied if

$$C_n=(-1)^n\sqrt{-2i}J_n\left[\delta\left(\frac{f}{\omega}+n\right)\right]\frac{A(0)^{1/4}h_{\mathrm{Ek}_n}(0)}{2\chi_n(0)h_{\mathrm{Ek}_0}(0)}. \tag{23}$$

For simplicity in presentation we assume that $A(z)$ does not vary significantly at $z = 0$ relative to the mode Ekman depth, that is, $\chi_n(0) \sim 1$, although we retain this factor in subsequent calculations.

The full solution is therefore given by

$$\mathbf{u}(z,t)=\frac{\boldsymbol{\tau}_w}{\rho\sqrt{fA(0)}}e^{-i(\pi/4)}\sum_{n=-\infty}^{\infty}\left\{(-1)^n\underbrace{\left(\frac{f}{f+n\omega}\right)^{1/2}J_n(\gamma_n)}_{\mathrm{I}}\underbrace{\Omega_n(z)}_{\mathrm{II}}\underbrace{e^{i[n\omega t+\gamma_n sin(\omega t)]}}_{\mathrm{III}}\right\}, \tag{24a}$$

where

$$\Omega_n(z)=\left[\frac{A(0)}{A(z)}\right]^{1/4}e^{-(1+i)\int_z^0 h_{\mathrm{Ek}_n}^{-1}(Z)\,dZ}, \quad \text{and} \tag{24b}$$

$$\gamma_n=\delta\left(\frac{f}{\omega}+n\right). \tag{24c}$$

Note that only the vertical structure functions [(24b)] are approximate, and in the case that A_ν is vertically uniform, this solution is exact.

The term outside the summation defines the standard Ekman velocity scale, as arises in the steady-state problem. This amplitude term then multiplies an infinite series of oscillating vertical modes, each with vertical structure determined by the boundary layer ordinary differential equation [(11)]. Term II [(24b)] defines the vertical structure of the individual modes, each of which is a solution to a steady-state Ekman problem with a modified rotational frequency of $f + n\omega$. Thus, higher modes are progressively more surface trapped, with boundary layer depth scale h_{Ek_n}. The extent of the vertical trapping of higher modes can be noted by considering that for the diurnal period considered here, mode $n = 2$ has a vertical depth scale less than that of a traditional Ekman layer at latitude 90°. It can be anticipated from this that, in the time periodic problem, oscillating A_ν leads to a shoaling of the mean flow relative to the constant A_ν solution (section 3c).

The value of the full summation in (24a) at $z = 0$ is determined by the surface boundary condition (6b); however, for a given value of δ some modes will be excited more than others. Term I of (24a) thus can be considered as determining how efficiently the wind stress projects onto each mode, with larger values of δ leading to more significant excitation of higher modes (Fig. 2). The ratio f/ω in γ determines the symmetry of modes that are excited, with $f/\omega \to 0$ leading to a symmetric excitation of positive and negative modes, whereas larger values of f/ω are skewed toward positive modes (Fig. 2). When $\delta = 0, J_0(0) = 1$ and $J_n(0) = 0$ for $n \neq 0$, such that only the zeroth Bessel function is excited, and the steady-state Ekman solution is recovered.

The time dependence in (24a), term III, is a complex, modulated oscillation (Fig. 3). Mathematically, the time dependence of each mode takes the form of a frequency-modulated signal, oscillating at frequency ω, with carrier frequency $n\omega$. This similarity can be exploited to rewrite (24a) with a simpler time dependence at the expense of a more complex expression for the mode amplitude and depth dependence:

$$\mathbf{u}(z,t)=\frac{\boldsymbol{\tau}_w}{\rho\sqrt{fA(0)}}e^{-i(\pi/4)}\sum_{l=-\infty}^{\infty}\left[\sum_{n=-\infty}^{\infty}(-1)^n\left(\frac{f}{f+n\omega}\right)^{1/2}J_n(\gamma_n)J_{l-n}(\gamma_n)\Omega_n(z)\right]e^{il\omega t}. \tag{25}$$

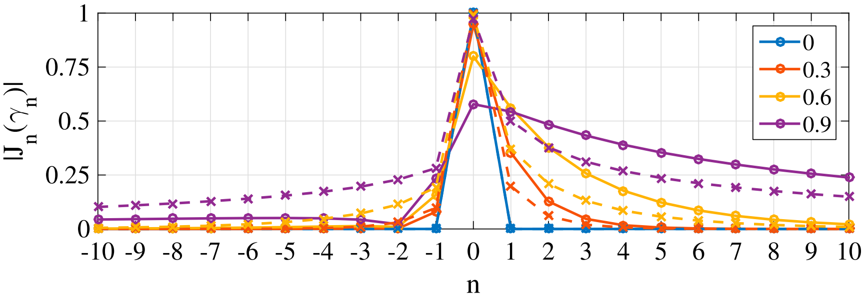

FIG. 2. Bessel function wind stress coupling coefficients for the first ±10 modes at 10° (dashed) and 50° (solid), for values of δ as indicated.

3. Discussion of solution

In this section, several pertinent aspects of the solution (24a) will be explored, including a quantitative formulation of the rectification of velocity and shear in the time-averaged solution.

a. *Qualitative solution characteristics*

Figure 4 shows an example solution hodograph, where it assumed that A_ν is elevated between 1800–0600 hours, with the daily minimum occurring at 1200 h. Velocity vectors trace closed contours over a 24-h period, the time average of which is shown (heavy black), and which can be compared to the steady-state Ekman solution (dashed black). Differences between these lines represent rectification of the diurnal variability in A_ν to the low-frequency velocity field. Understanding and quantifying these rectification effects is the focus of section 3c below.

Further insight into the solution comes from considering the solution in the time–depth plane. Figure 5 shows an example solution for a midlatitude Ekman layer forced by a constant zonal wind stress. In the early morning hours, A_ν is high, and the Ekman layer is at its deepest. As A_ν decreases toward its midday minimum, the Ekman layer begins to shoal, most clearly evident in the shoaling of the zero zonal velocity line from $z \sim -h_{\mathrm{Ek}_0}$ to $z \sim -0.5h_{\mathrm{Ek}_0}$. A surface-intensified diurnal jet develops (Price et al. 1986), associated with a high shear, near-surface layer. Below this high shear region, weak, anticyclonic oscillations, with upward-propagating phase, begin. In the near-surface ocean, near-inertial variability with upward-propagating phase is often attributed to inertial waves with downward energy propagation. However, the one-dimensional nature of the solution considered here precludes the existence of internal waves. Instead these features should be interpreted as inertial oscillations, with phase propagation determined by the diurnal cycle in viscosity, as discussed further below.

The primary zonal momentum balance throughout the diurnal evolution is between the Coriolis acceleration $-fv$ and the turbulent momentum flux convergence $(A_\nu u_z)_z$, consistent with Ekman layer dynamics (Fig. 6). Near the surface, there is an alternating acceleration and deceleration of the flow on either side of the diurnal jet maximum, necessary to maintain the classic Ekman transport as the Ekman depth shoals and deepens. Deeper in the layer, there are upward-propagating signals in acceleration that are balanced largely by the Coriolis acceleration, a signature of inertial oscillations. These features can thus be interpreted as inertial oscillations initiated by the loss of Ekman balance caused by the decreasing midday A_ν. In this manner, they are similar to the inertial oscillations observed in simple models of the nocturnal, low-level jet in the atmospheric boundary layer, where it is found that a layer that abruptly transitions from viscid to inviscid dynamics, representing the change between daytime and nighttime conditions, causes inertial

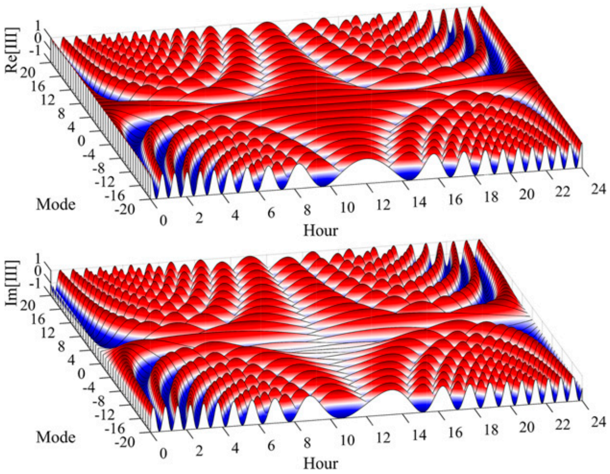

FIG. 3. Time dependence for the first ±20 modes, assuming $\delta = 0.75$, and latitude 45°. (top) Real and (bottom) imaginary components.

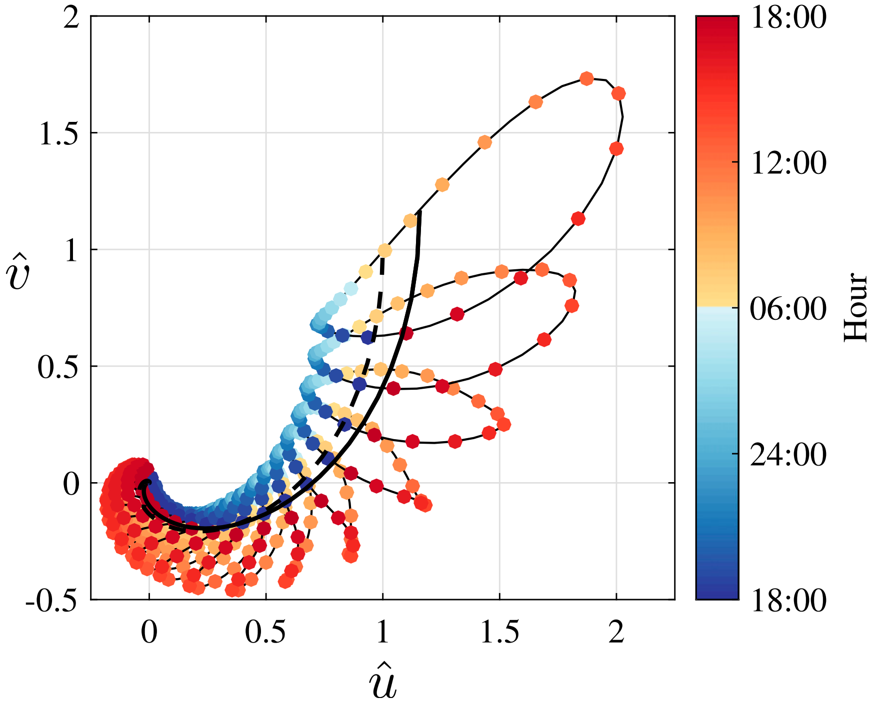

FIG. 4. Example diurnal cycle velocity hodograph for steady wind stress and vertically uniform A_ν, with $h_{\text{Ek}} = 14$ m and $\delta = 0.75$. At each depth, the velocity vector traces a closed contour over one 24-h period, plotted for selected depths, beginning at $z = 0$ and decreasing in increments of 2m (thin lines, with color scale indicating hour of day). The time-averaged diurnal velocity is shown (heavy black), as is the steady-state solution (dashed black). All velocities are normalized by the steady-state Ekman surface velocity.

oscillations around the equilibrium solution (Blackadar 1957; Van de Wiel et al. 2010). The model considered here is not completely inviscid at depth, but, by analogy with atmospheric low-level jets, leads to inertial oscillations that progressively shoal, following the shoaling Ekman layer.

Figure 7 compares a more realistic simulation from a 1D model forced by a diurnal cycle in surface buoyancy fluxes (appendix A), utilizing the KPP turbulence parameterization (Large et al. 1994). The right panels show the time periodic theoretical solution, forced by the same surface wind stress, using values of A_ν diagnosed from the numerical model output. The boundary value problems, (11), are solved numerically for simplicity and accuracy, rather than using the WKBJ approximation [see Wenegrat and McPhaden (2016) for a discussion of the use of the WKBJ approximation for $A_\nu(z)$ based on similarity theory]. Major features are well reproduced, including the near-surface diurnal jet, middepth minima in zonal velocity, descending shear layers, suppressed nighttime shear, and enhancement of shear near the base of the turbulent boundary layer. Other features that are not well reproduced are the stronger inertial oscillations below the boundary layer evident in the numerical model, and the deep evolution of the descending diurnal shear layers, whose descent slows in the numerical model relative to the theoretical prediction. These features are likely attributable in part to the lack of internal wave radiation in the 1D model configuration, and the space–time coupling of turbulent viscosity in KPP, respectively.

b. *Parameter dependence*

In this section, the parameter dependence of the solution (24a) will be explored to illustrate how the dynamics evolve across different regimes. The aspects of the solution unique to the diurnal cycle are evidently controlled by only two nondimensional parameters: δ, the strength of the diurnal A_ν cycle [(7)], and f/ω, the ratio between the local inertial frequency and the period of the eddy viscosity. Figure 8 illustrates the modification of boundary layer currents as δ is varied. Increasing δ increases the strength of the near-surface diurnal jet, as expected from the momentum balance discussed above. The strength, and location, of the inertial oscillations are also affected, with increasing δ leading to higher velocities, occurring closer to the surface and slightly later in the day. Similarly, with

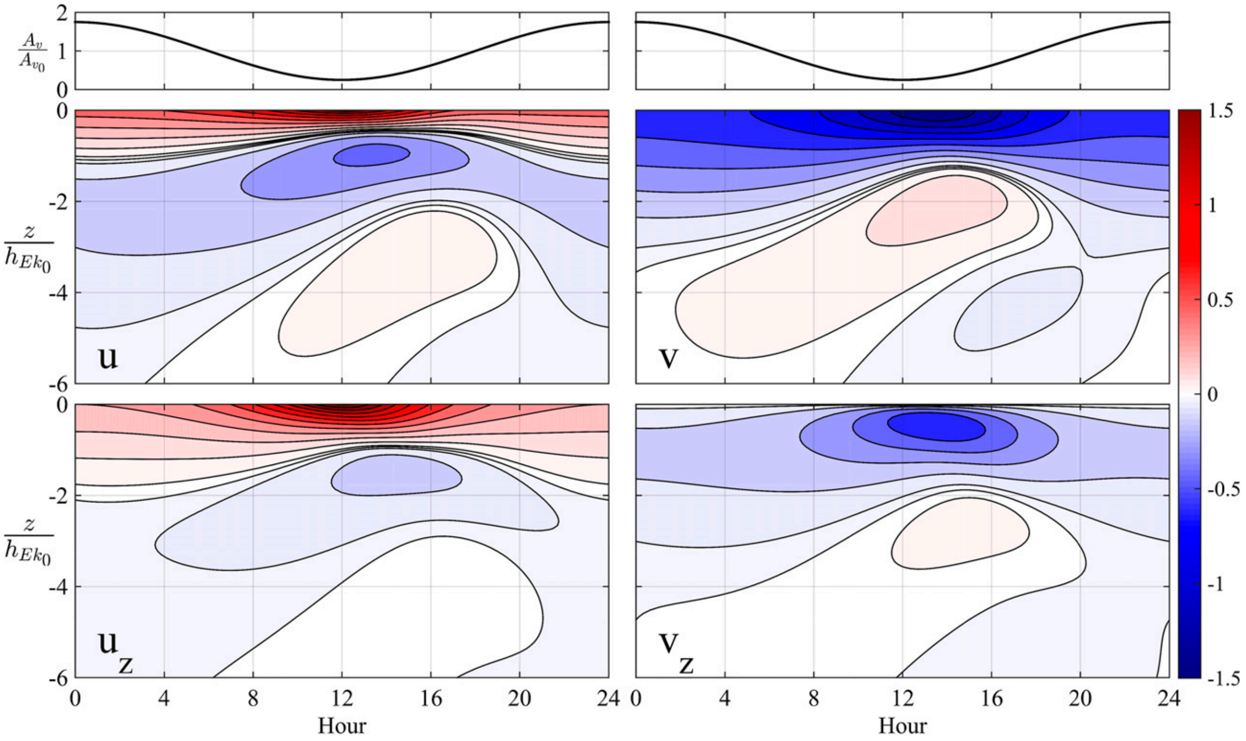

FIG. 5. Modeled diurnal cycle at 45°N, for vertically uniform A_ν, and $\delta = 0.75$. Velocities are normalized by $\tau/(\rho\sqrt{fA_{\nu_0}})$, and shear is normalized by $2\tau/(\rho A_{\nu_0})$, twice the surface shear for the constant viscosity solution. Contours are nonlinearly spaced to emphasize the deep variability.

higher δ the enhanced near-surface shear persists later in the day, with evident subsurface maxima occurring several hours after the daily minimum in A_ν.

Figure 9 compares the effect of varying latitude, holding δ constant. At low latitudes an afternoon deepening of the sheared diurnal jet is evident, whereas the near-surface velocity and shear response becomes increasingly symmetric around the midday minimum in A_ν as latitude increases. Deeper in the layer, $z \sim -4h_{\mathrm{Ek}_0}$, the diurnal modulation becomes increasingly pronounced as latitude increases. An upward-propagating inertial oscillation is only clearly evident for 45°, which may result from the inability of the periodic domain considered here to support inertial oscillations for latitudes less than 30°, where the inertial period exceeds 1 day. These effects are a consequence purely of varying latitude, while holding A_ν fixed, and are therefore separate from those arising due to the horizontal

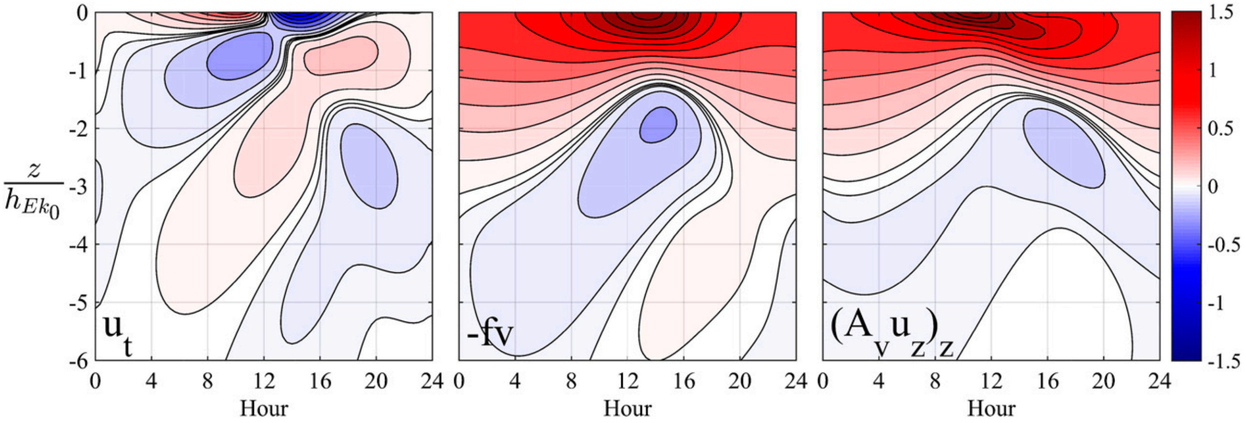

FIG. 6. Zonal momentum balance terms for the same case considered in Fig. 5, with values normalized by $\tau/(\rho h_{\mathrm{Ek}_0})$.

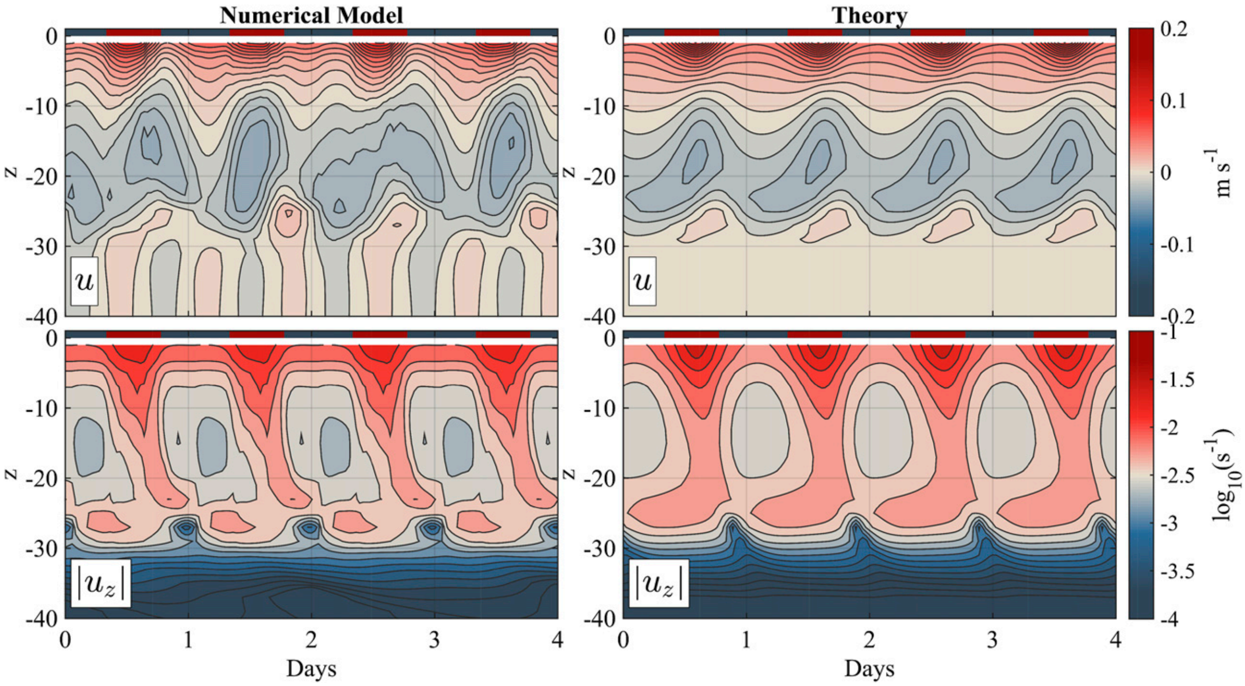

FIG. 7. Comparison of (left) numerical model and (right) theoretical solution for 45°N, with $\tau = 0.1\,\mathrm{N\,m^{-2}}$. Parameters for the theoretical solution are diagnosed from the numerical solution following the discussion in appendix A, and the boundary value problems, (11), are solved numerically rather than utilizing the WKBJ approximate solution. Times of negative (red) and positive (blue) net surface buoyancy flux are indicated in each plot for $z > 0$.

component of the Coriolis force, which has been shown to modify boundary layer flow through altering the turbulence intensity and Reynolds stress (Zikanov et al. 2003; McWilliams and Huckle 2006).

The diurnal evolution is also affected by the vertical structure of A_ν (Fig. 10), as illustrated by a comparison between the solution for a vertically uniform A_ν profile and a more realistic modified Gaussian profile (Zikanov

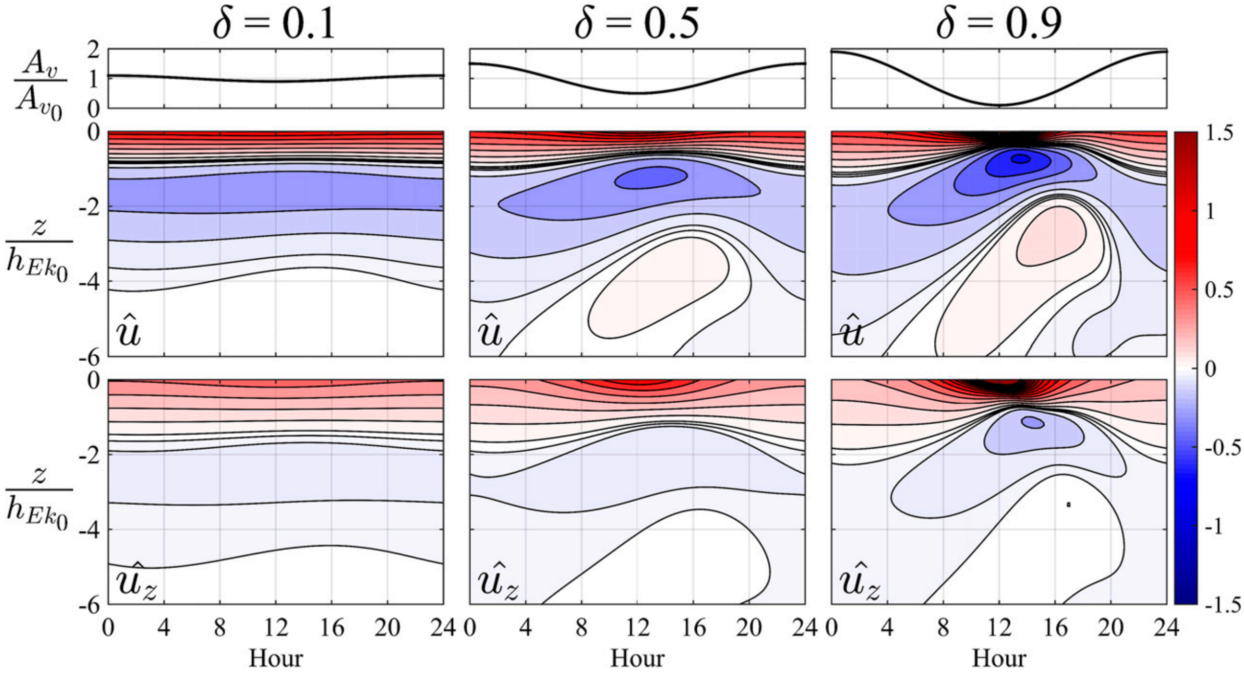

FIG. 8. Effect of varying δ with parameters and normalization as given for Fig. 5.

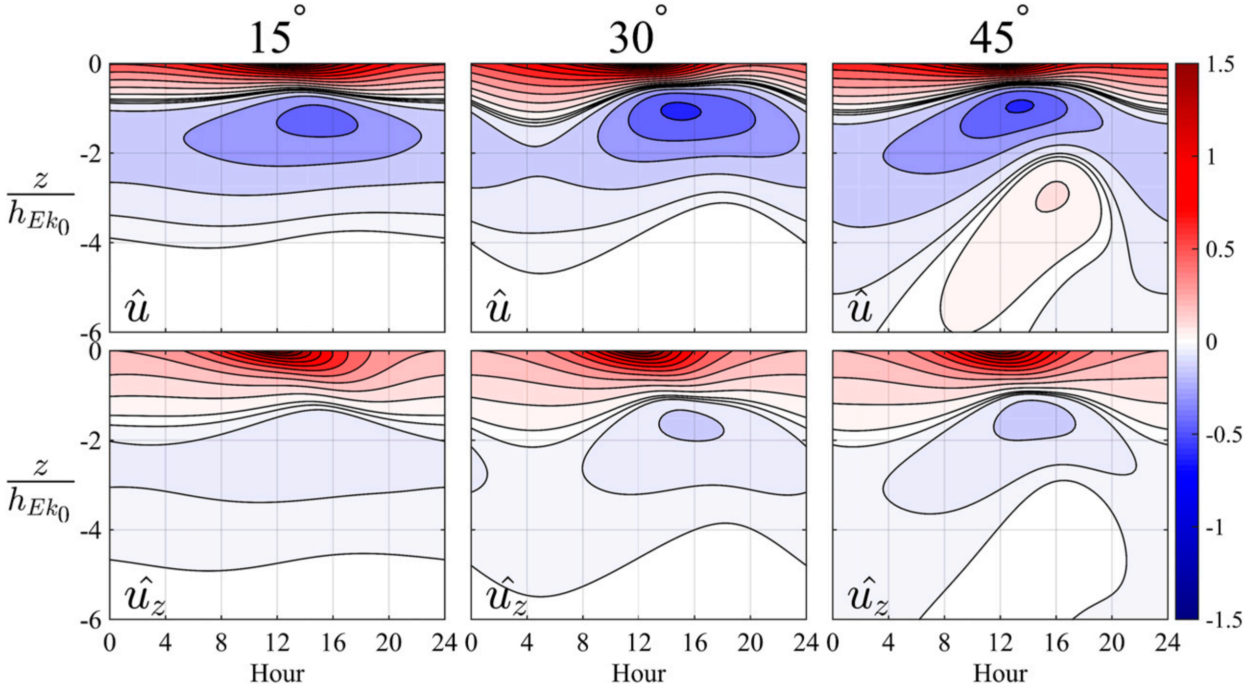

FIG. 9. Effect of varying latitude, with parameters and normalization as given for Fig. 5. Note both the velocity and depth normalizations are a function of latitude.

et al. 2003). The basic Ekman layer structure is stretched vertically according to the vertical structure of A_ν, consistent with the interpretation of the integral in (24b) as a stretching of the vertical coordinate based on a vertically localized Ekman depth, as discussed in Wenegrat and McPhaden (2016). This leads to an enhancement of shear in the near-surface, as well as deeper in the layer ($z < -0.5h_{\mathrm{Ek}}$), for the modified Gaussian profile, which has reduced A_ν in these depth ranges. Near $z = -0.25h_{\mathrm{Ek}}$, the isolines of velocity undergo more pronounced diurnal oscillations for the modified Gaussian profile, following the discussion in section 3a (Fig. 6), where it is suggested that inertial oscillations are generated following the shoaling of the Ekman layer, with vertical phase speed determined by $\partial h_{\mathrm{Ek}}(z)/\partial t$, which for a given value of δ will be enhanced for larger values of A_ν.

c. Rectification

Diurnal variability poses a challenge for the interpretation of observational data in terms of Ekman dynamics, as observations are frequently averaged in time in order to improve the signal-to-noise ratio and remove other forms of variability. Understanding the effect of time variability in A_ν is thus critical to understanding time-averaged observations. Integrating the time-dependent solution [(24a)] over one diurnal cycle allows for comparison with the steady-state solution ($\delta = 0$), which can be used to examine the rectification effects of the diurnal cycle in mixing. We define a diurnal average of a quantity $X(t)$ as

$$\langle X \rangle = \frac{\omega}{2\pi} \int_0^{2\pi/\omega} X(t)\,dt\,. \tag{26}$$

The solution for velocity averaged over one diurnal cycle is given by

$$\langle \mathbf{u}(z) \rangle = \frac{\boldsymbol{\tau}_w}{\rho\sqrt{fA(0)}} e^{-i(\pi/4)} \sum_{n=-\infty}^{\infty} \left[\left(\frac{f}{f + n\omega} \right)^{1/2} J_n^2(\gamma_n) \Omega_n(z) \right]. \tag{27}$$

This takes on a particularly simple form at the surface where

$$\langle \mathbf{u}(0) \rangle = \frac{\boldsymbol{\tau}_w}{\rho\sqrt{fA(0)}} e^{-i(\pi/4)} \sum_{n=-\infty}^{\infty} \left[\left(\frac{f}{f + n\omega} \right)^{1/2} J_n^2(\gamma_n) \right]. \tag{28}$$

As discussed above, the projection coefficients decrease quickly with increasing mode number due to the rapid rolloff of the squared Bessel functions J_n^2 and the dependence on $[f/(f + n\omega)]^{1/2}$, which is small for large absolute values of n. Thus, the time average solution for velocity will be dominated by the low modes.

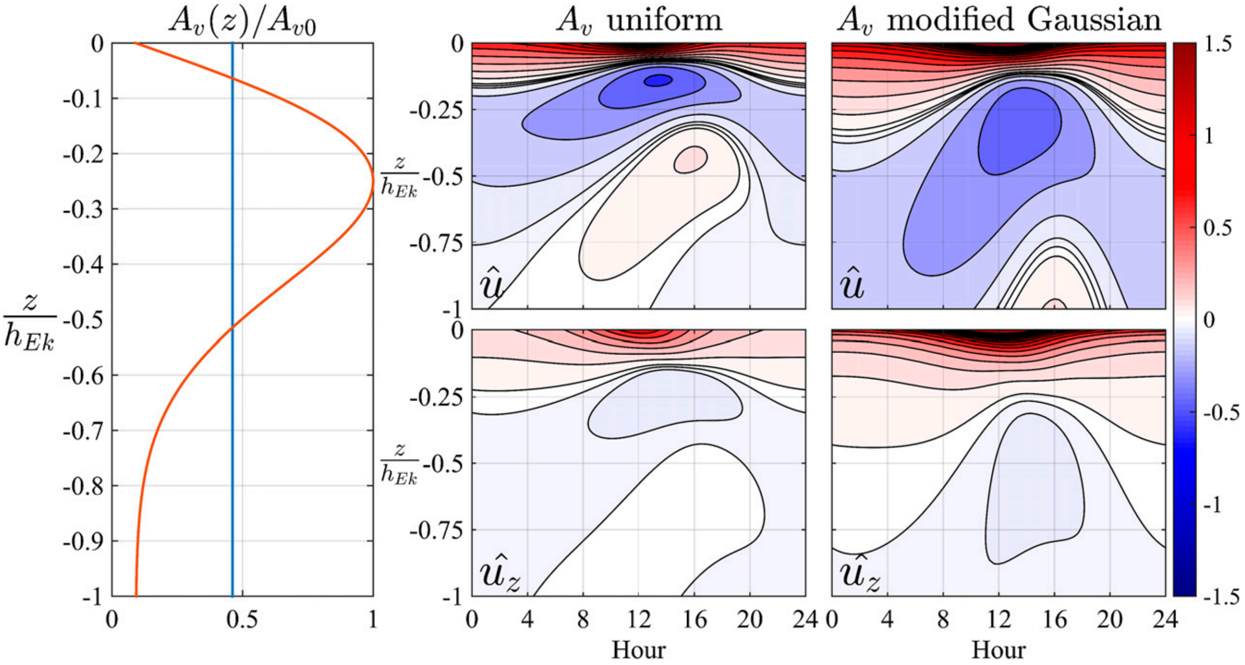

FIG. 10. Vertical structure in A_ν modifies the diurnal cycle solutions. Right panels are for a modified Gaussian A_ν profile $[A_\nu(z) = A_{\nu_0} e^{-0.5(z/0.25h_{\rm Ek})} + \varepsilon$, orange line in left plot], and center panels are for a vertically uniform A_ν, taken as the mean value of the modified Gaussian profile between $z = 0$ and $z = -h_{\rm Ek}$ (blue line in left plot). The vertical coordinate is normalized using $h_{\rm Ek} = 0.7\sqrt{\tau/\rho}/f$, velocity is normalized by $\tau/(\rho\sqrt{fA_{\nu_0}})$, shear is normalized by $4\tau/(\rho A_{\nu_0})$, and $\delta = 0.75$. Solutions to (11) were found numerically.

It is worth noting that the summation in (28) can have an imaginary component, arising from modes where $(f + n\omega) < 0$. This can lead to a rotation of the surface velocity relative to the 45° deflection predicted by steady-state Ekman theory, as shown in Fig. 11 as a function of the controlling parameters. Modifications to the direction of the surface current resulting from diurnal variability in A_ν are generally quite small (<10°), in the downwind direction, and are hence not likely to be a significant factor in explaining discrepancies between observed surface current deflections and the predictions of classic Ekman theory (Huang 1979). This effect, arising solely from temporal variability in A_ν, is, however, distinct from the changes in the direction of wind-driven flow that result from vertical structure in A_ν, through (20), which can introduce significant changes in the direction of the ageostrophic flow.

In a similar manner, the solution for surface shear averaged over one diurnal cycle can be found by vertically differentiating (27) and evaluating at $z = 0$:

$$\langle \mathbf{u}_z(0) \rangle = \frac{\boldsymbol{\tau}_w}{\rho A(0)} \sum_{n=-\infty}^{\infty} J_n^2(\gamma_n). \tag{29}$$

The higher modes will contribute more to the time average shear solution than they do to the time-averaged velocity, which will lead to larger rectification effects, emphasizing how surface velocity and shear will have different responses to a diurnal cycle in turbulent mixing, a result that is independent of the vertical structure of A_ν. Further, the quantity in the summation

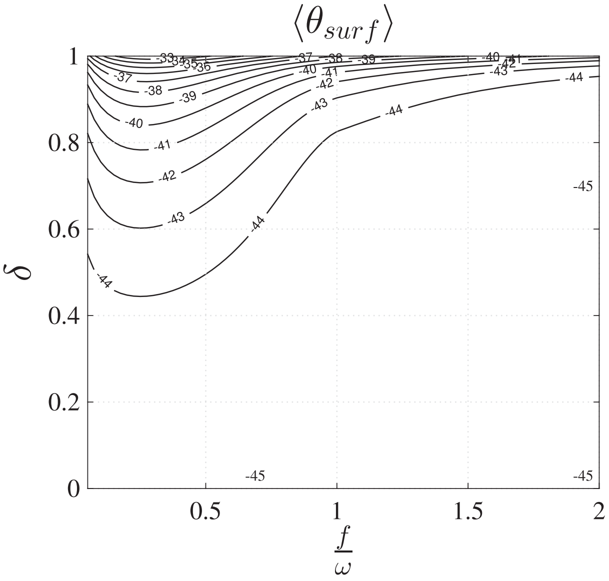

FIG. 11. Angle of the time-averaged surface currents relative to the surface wind stress. Negative values indicate anticyclonic rotation.

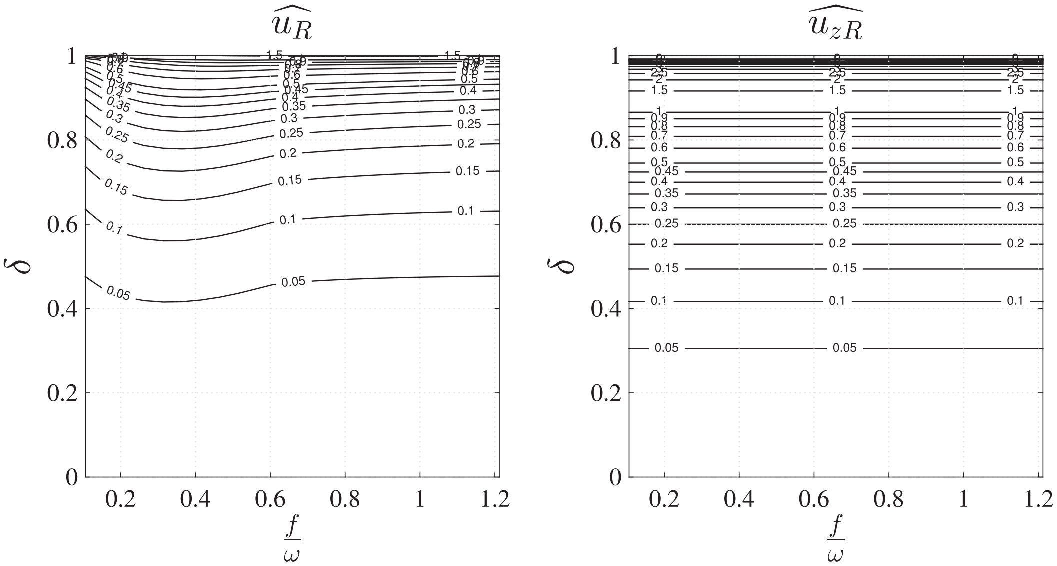

FIG. 12. Contour plot of the parameter dependence for the theoretical normalized rectification values [(30)] for (left) velocity and (right) shear.

is positive definite; hence, rectification of diurnal variability will always enhance the mean surface shear relative to the steady-state Ekman problem, indicating a shoaling of the mean, wind-driven flow.

A simple normalized measure of rectification, for a variable X, can be defined as

$$\hat{X}_R = \frac{\left||\overline{X}| - |\langle X\rangle|\right|}{|\overline{X}|}, \tag{30}$$

where angle brackets as before represent averaging over the diurnal cycle and the bar notation represents the steady-state solution, assuming no time variability in A_ν ($\delta = 0$). This measure of rectification, (30), can then be applied to modeled and theoretical values of velocity and shear to assess the degree of rectification, giving

$$\widehat{u_R}\big|_{z=0} = \left|1 - \left|\sum_{n=-\infty}^{\infty}\left(\frac{f}{f+n\omega}\right)^{1/2} J_n^2(\gamma_n)\right|\right|, \tag{31}$$

and,

$$\widehat{u_{zR}}\big|_{z=0} = \left|1 - \sum_{n=-\infty}^{\infty} J_n^2(\gamma_n)\right|, \tag{32}$$

as shown in Fig. 12. Velocity rectification increases with increasing δ, with reduced rectification effects at low latitudes, due in part to the enhanced total velocities in the Ekman solution as $f \to 0$. Shear rectification is essentially latitude independent, which can be anticipated from (32), with a rapid increase at high δ and maximum values of $\widehat{u_{zR}} \gg 10$ as $\delta \to 1$. Thus, while both velocity and shear are subject to rectification effects at all latitudes, the vertical structure of the time-averaged currents is more sensitive than their magnitude to time variability in A_ν.

As a basic confirmation of this parameter dependence, we compare the approximate theory to a numerical solution that does not impose the same constraints on periodicity. To do this, we numerically solve (2) for an initially motionless ocean forced by a constant zonal wind stress, with a sinusoidally varying A_ν, using a finite-element Galerkin method (Skeel and Berzins 1990). Model integrations are carried out for 50 days and averages are taken over the last half of the integration. Rectification in this idealized model can be seen to follow closely to the theoretical prediction (Fig. 13). This result holds regardless of latitude, suggesting the time periodic domain is not unduly influencing this result. Comparisons to a more complete numerical model are presented in appendix A.

One additional consequence of the changes in the time-mean solution introduced by time variability in A_ν is that the time-mean current no longer directly satisfies a steady-state Ekman solution. It can thus be anticipated that in order to effectively fit a steady Ekman layer solution to the resulting currents it will be necessary to define an "effective" A_ν, which may differ significantly from the mean of the time-varying values, a result familiar from previous work on Ekman layer rectification (McWilliams et al. 2009).

Following McWilliams et al. [2009, (19)–(21)], we define a complex, depth-dependent, effective eddy viscosity $\mathbf{A}_{\nu_{\mathrm{Eff}}}$ that fits the time-averaged diurnal solution to a steady-state Ekman model. Namely,

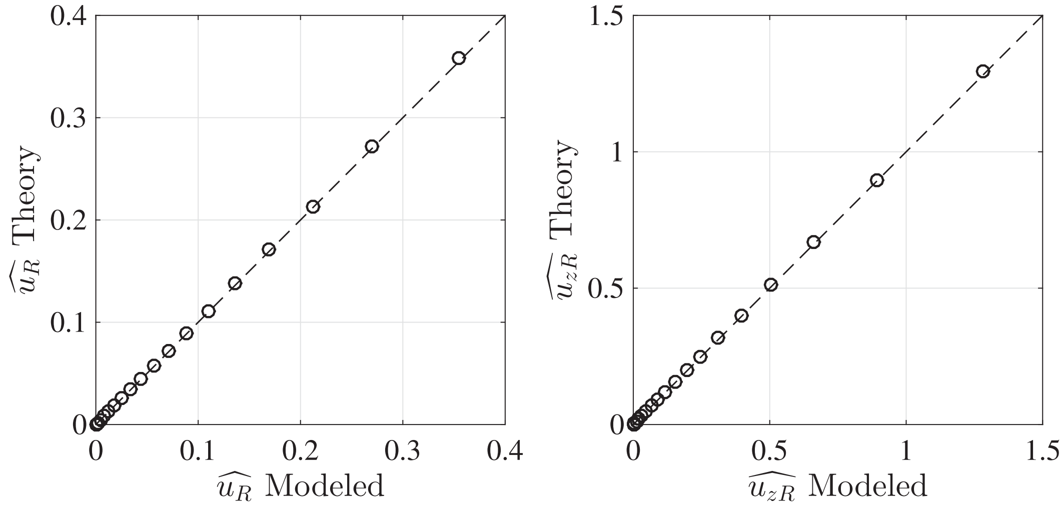

FIG. 13. Validation of the rectification implied by the time periodic solution against a numerical solution of the initial boundary value problem as discussed in section 3c.

$$\mathbf{A}_{\nu_{\text{Eff}}}(z) = \frac{\int_{-\infty}^{z} if\langle\mathbf{u}\rangle\,dz}{\langle\mathbf{u}\rangle_z}, \tag{33}$$

such that

$$if\langle\mathbf{u}\rangle = [\mathbf{A}_{\nu_{\text{Eff}}}(z)\langle\mathbf{u}\rangle_z]_z. \tag{34}$$

This is shown for a diurnal cycle of A_ν that is uniform in depth, which more clearly illustrates the modifications arising solely from diurnal variability (Fig. 14). The diurnal cycle of A_ν leads to a reduction in near-surface $|\mathbf{A}_{\nu_{\text{Eff}}}|$, necessary to generate the enhanced near-surface shears. In all cases there is a middepth maximum of $|\mathbf{A}_{\nu_{\text{Eff}}}|$, which moves deeper for increasing values of δ (off vertical scale for $\delta \geq 0.75$). Positive rotation angles of the effective viscosity indicate that the diurnally averaged stress is rotated cyclonically relative to the local mean shear, consistent with observations (Price and Sundermeyer 1999; Lenn and Chereskin 2009), and numerical models (McWilliams et al. 2009). These results can be compared to those from McWilliams et al. (2009, their Fig. 20), which follow a similar overall structure, suggesting that the rectification mechanisms captured here are relevant to the more complete model physics considered therein.

4. Summary

In this work, we have presented a simple theoretical model of the time-dependent Ekman layer with time periodic eddy viscosity, intended as a basic approximation of the complex and interdependent processes governing the real evolution of the ocean surface boundary layer under time-varying forcing (section 2). This model has the advantage of simplicity, illustrating the basic physics of how time variability in mixing changes the ocean response to a surface wind stress (section 3), and rectifies to the time-mean solution (section 3c). This simplicity comes at the trade-off of physical realism, particularly so in the constraints placed on the vertical and temporal structure of eddy viscosity and that the turbulent viscosity is not allowed to evolve as a function of the resulting near-surface shear flows. The utility of this model can thus be viewed principally as a means of building physical insight and isolating processes that do not rely on these feedback mechanisms to occur, as, for instance, is discussed in regards to the time-mean effective eddy viscosity found in section 3c. It can thus be considered similar to approaches adopted in the atmospheric sciences literature on the dynamics of nocturnal low-level jets (Blackadar 1957; Buajitti and Blackadar 1957; Sheih 1972).

As guidance for the interpretation of observations, several conclusions can be drawn directly from the work presented here. The discussion of section 2 hints at the complexity of trying to infer the true A_ν from measurements of interior velocities or boundary flux values (Wenegrat et al. 2014), which in general will require the solution of a nonlinear equation (cf. Cannon 1984). This is the subject of a large body of literature on inversion techniques for the one-dimensional heat equation, which have not been systematically applied to the oceanic problem. The common approach of fitting steady-state Ekman models to time-averaged fields can be expected to

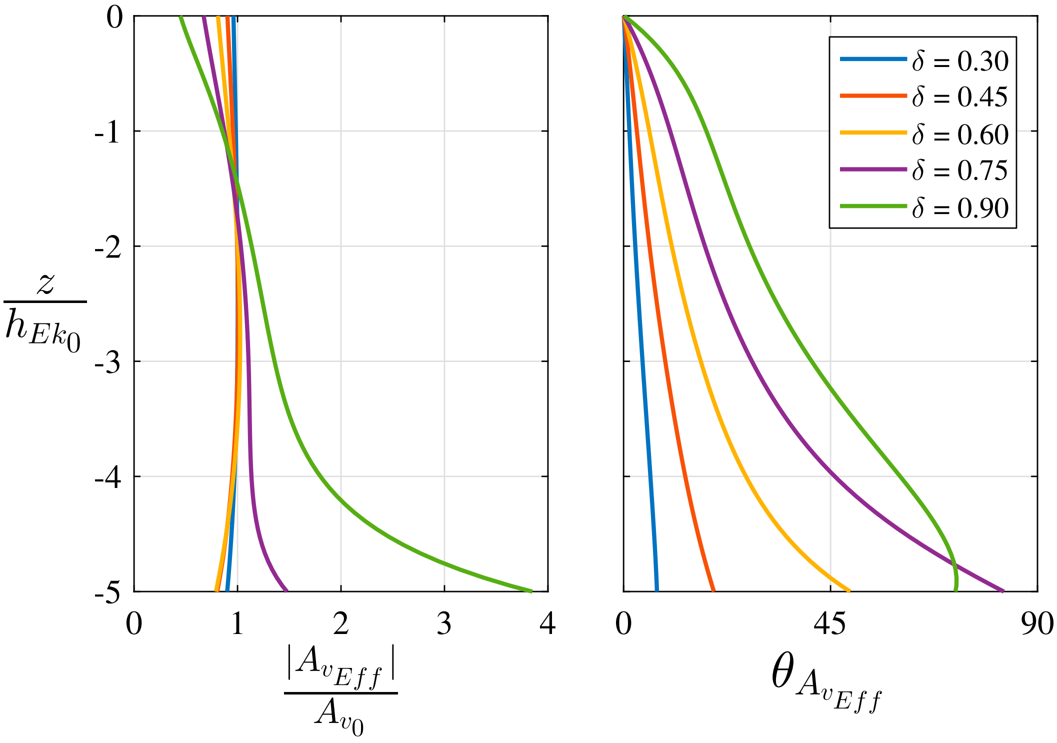

FIG. 14. Effective eddy viscosities inferred from the time-mean solution for vertically uniform A_ν, as defined by (33), with various δ values as shown in the legend; $A_{\nu_{\mathrm{Eff}}}$ magnitudes are normalized by the true A_ν, and angles (°) are relative to the local mean shear direction.

result in values of A_ν, possibly complex, which depart significantly from the true values, complicating their physical interpretation and limiting their utility. This follows directly from changes in the mean vertical structure of the time-dependent solution, without requiring any feedback mechanism between shear flow and A_ν, providing a simple explanation of observations (Price and Sundermeyer 1999; Lenn and Chereskin 2009) that differs somewhat in interpretation from previous investigations (McWilliams et al. 2009).

Time variability in A_ν modifies both the velocity and vertical structure of ocean currents, and these changes rectify to the low-frequency flow. Velocity shear is more strongly rectified than velocity, and in both cases the magnitude of the rectification is only weakly dependent on latitude and dominated by the strength of the periodic variations in mixing. The Ekman solution is nonlinearly dependent on A_ν, and, as demonstrated here, even periodic time variations in A_ν, which introduce no change to the time-mean value, can greatly modify the mean boundary layer flow. Finally, we note that the upward-propagating inertial oscillations that appear in our solution (Fig. 6) are forced by the diurnal cycle in viscosity, with the vertical phase propagation speed determined by the rate at which the diffusive boundary layer shoals. The dynamics of these oscillations are exactly those implicated in the creation of atmospheric nocturnal jets (Van de Wiel et al. 2010) and importantly represent a physical mechanism by which a steady wind stress forcing, in the presence of a time-varying solar heat flux, can excite near-inertial motions. However, their presence in the oceanic boundary layer is less clearly documented and hence deserves further investigation.

Acknowledgments. The authors thank Ren-Chieh Lien and Stephen C. Riser for helpful comments on an earlier version of this manuscript and two anonymous reviewers for their comments. PIRATA mooring data are available online (through http://www.pmel.noaa.gov/tao/). The authors also thank NOAA for support of this study as well as the Joint Institute for the Study of the Atmosphere and Ocean (JISAO) under NOAA Cooperative Agreement NA15OAR4320063.

APPENDIX A

Numerical Model

In addition to the basic numerical solution discussed in section 3c, we utilize the MITgcm (Marshall et al.

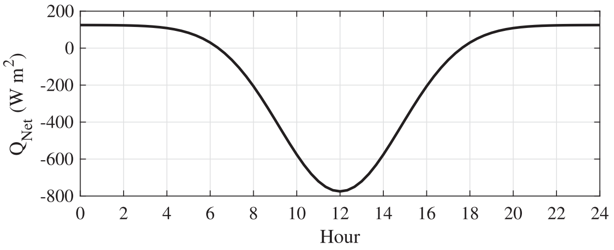

FIG. A1. Idealized diurnal cycle of net surface heat flux used to force the numerical model discussed in appendix A.

1997) run in an idealized, one-dimensional configuration with 2-m vertical resolution, spanning from $z = -500$ to 0 m. This resolution is sufficient to resolve the Ekman layer in all simulations used. The model is initiated from a state of rest with a weak, vertically uniform, temperature stratification, equivalent to $N^2 = 2 \times 10^{-5}\,\mathrm{s}^{-2}$ ($T_z = 0.01°\mathrm{C\,m}^{-1}$). A two-component surface buoyancy flux is imposed, consisting of incoming shortwave radiation that is absorbed using a Jerlov type 2 absorption profile (Jerlov 1976) and an outgoing surface flux, held steady in time. The idealized diurnal cycle is thus a repeating cycle of a function given by

$$Q_{\mathrm{SWR}}(t) = -Q_0 e^{-[(\hat{t}-0.5)/0.25]^2}, \qquad \text{(A1)}$$

where $Q_0 = 900\,\mathrm{W\,m}^{-2}$, and $\hat{t}$ ranges from 0–1 daily. A constant outgoing surface heat flux is given by $Q_{\mathrm{LW}} = 125\,\mathrm{W\,m}^{-2}$. This particular profile leads to ~11 h of heat flux into the ocean (Fig. A1), which is an idealization taken to facilitate comparison between the model results and theory. These surface fluxes are used for all runs, which ignores variations in solar heat flux as a function of latitude and season that generally may result in variability at frequencies other than the diurnal. Also important to note is that this forcing profile leads to a net heat flux into the ocean, which in the 1D configuration utilized here can only lead to increasing temperature stratification at the base of the turbulent boundary layer, affecting the evolution of the turbulent boundary layer depth. This can be accounted for by imposition of a restoring interior heat flux (as in McWilliams et al. 2009); however, as we are here simply comparing the theory to the model based on diagnosed fields and are not concerned with the detailed evolution of the turbulent boundary layer depth, we do not impose additional sources of interior cooling.

Surface wind stress is steady and in the zonal direction. The magnitude of the surface wind stress is varied across runs, while the surface heat flux profile (Fig. A1) is not varied. This leads to variations in the strength of the diurnal mixing cycle between runs. Turbulent viscosity is parameterized using KPP (Large et al. 1994), and calculated viscosities are output at every time step. The calculation of surface layer viscosities in KPP couples vertical structure and time dependence, providing a more realistic model of near-surface turbulence than the simple dependence we require in section 2. All model integrations are performed for 100 days with a 20-min integration time step.

The model output is principally useful as a point of qualitative comparison, as in Fig. 7. However, it is also possible to provide at least a basic assessment of the rectification effects discussed in section 2c. To do this we run the above model repeatedly, varying latitude from 5°–90° in 5° increments and wind stress $\tau = 0.1$–$0.4\,\mathrm{N\,m}^{-2}$, holding the diurnal surface buoyancy flux profiles constant across runs. In KPP the coupling of space–time variability in A_ν means there is no principled manner to affect the decomposition in order to estimate a steady-state solution for calculation of rectification values. Here, we make the simple ad hoc assumption that the vertical structure can be taken as the time average $A_\nu(t)$ over the last half of the integration period. We then estimate δ by fitting a diurnally periodic sine function to the average A_ν in the turbulent surface boundary layer. Using these two estimates, it is possible to compare the estimated rectification to the theory.

Figure A2 shows the resulting estimate of the δ parameter for all model runs. There is a general increase in δ at low latitudes, emphasizing that this comparison is not an exhaustive exploration of the parameter space. Lower values of δ at any given latitude could be achieved by decreasing the diurnal variations in surface heat flux or increasing the surface wind stress. For KPP, the error in approximating $A_\nu(z, t)$ as $K(t)A(z)$ at a fixed depth z is a complex, nonmonotonic function of both δ and $z/\overline{h}$, the ratio of z to the time-mean turbulent boundary layer depth. However, some insight into the limits of this decomposition comes from writing $A_\nu(z, t) = K(t)A(\sigma)$, where $\sigma = -z/h(t)$ is the rescaled vertical coordinate with a time-varying turbulent boundary layer depth $h(t)$. Approximating this in a Taylor series gives $A_\nu(z, t) \approx K(t)[\overline{A(z)} + \partial A/\partial t|_{t=t_0}(t - t_0)]$, where the bar notation indicates the time-mean value, which occurs at time t_0. The assumption of space and time separability can then be posed as an assumption that $(t - t_0)\partial A/\partial t|_{t=t_0} \ll \overline{A(z)}$ or, equivalently, $(t - t_0)\partial A/\partial \sigma|_{t=t_0}\, \partial \sigma/\partial t|_{t=t_0} \ll \overline{A(z)}$. Thus, at a given depth, both the local vertical slope of the eddy viscosity as well as the time rate of change of the boundary layer depth will affect the errors in approximating the eddy viscosity in KPP as separable in time and space.

Despite these limitations, we find velocity rectification in the numerical model is reproduced remarkably well

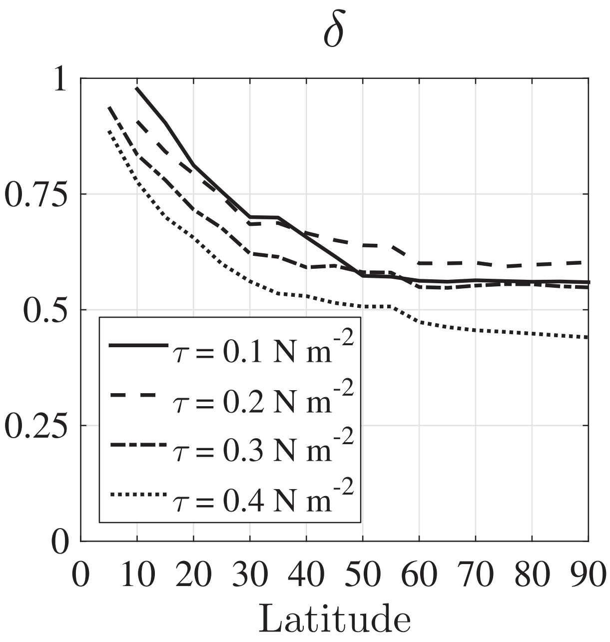

FIG. A2. Diagnosed magnitude of the diurnal A_ν cycle from the numerical model, calculated as described in appendix A, as a function of latitude and surface wind stress (legend).

by the theory (Fig. A3); however, shear rectification is greatly overestimated for values of $\delta > 0.8$. Several reasons for this are suggested. First, the method of estimating δ is somewhat arbitrary, and, for instance, the coupling of spatial structure and time dependence in KPP means that near-surface A_ν is generally subject to smaller diurnal fluctuations than deeper in the boundary layer. Shear rectification is particularly sensitive at high δ (Fig. 12) and hence may be particularly sensitive to incorrect estimates of this parameter. Second, higher vertical modes contribute more strongly to shear rectification than velocity rectification. These higher modes, with their small vertical scale and associated strong shear, may be damped in a more realistic turbulence closure such as KPP, where wind-driven shear feeds back into the determination of A_ν. Finally, for the surface forcing used here, the cases of high δ tend to occur at low latitudes (Fig. A2), associated with the deeper boundary layers in KPP generated in response to periodic buoyancy forcing at low latitudes (McWilliams et al. 2009), which results in the increasingly nonsinusoidal time variability of A_ν. Hence, some of the departure of the model results from the theory may implicate the time-varying structure of A_ν as departing from the basic theoretical assumptions.

APPENDIX B

Errors for $f + n\omega \rightarrow 0$

As discussed in section 2, application of the WKBJ approximation requires that $\mathrm{Ek}_n = A_0/[(f + n\omega)D^2]$ remains small, so as to not violate (16) and (17). In this appendix, we assess the error contributed to the total solution from the modes where $f \rightarrow \pm n\omega$, where mode $\mp n$ will have $\mathrm{Ek}_n \rightarrow \infty$. For the diurnal frequency considered here, this can occur only for modes $n = \pm 1, 2$ at latitudes 30° and 90°, respectively.

Each approximate solution for the vertical structure function (24b) can be considered as $\Omega_n = \hat{\Omega}_n + E_n$, where the hat notation indicates the exact solution and E_n represents errors associated with the WKBJ approximation. For the WKBJ approximation, $E_n \sim \mathrm{Ek}_n^{1/2}$. Utilizing this in the full summation, the error that the

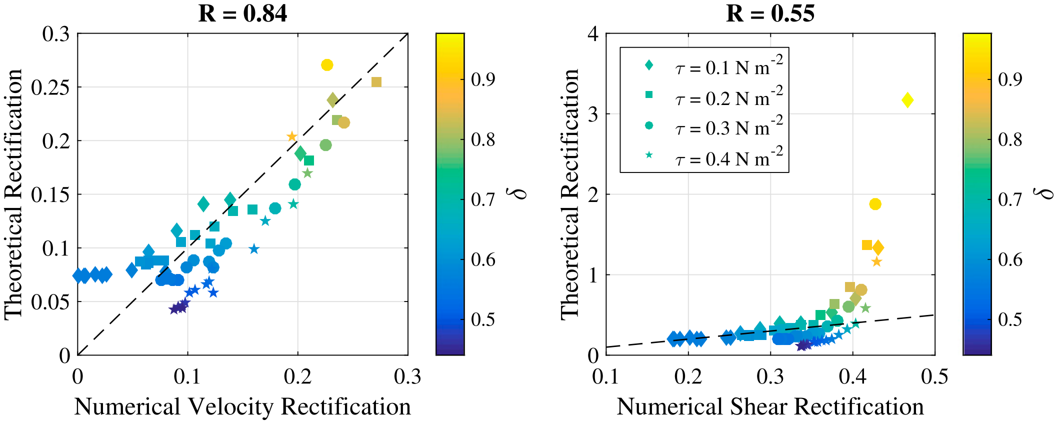

FIG. A3. Comparison of inferred rectification in the numerical model against theoretical predictions for (left) velocity and (right) shear. In each plot, color scale gives the inferred δ, the symbol shape gives the magnitude of the surface wind stress as shown in the legend, and the dashed line indicates the 1–1 line. Correlation coefficients are shown above each plot.

nth mode contributes to the total solution, which we denote E_{T_n}, will be proportional to

$$E_{T_n} \sim \left(\frac{f}{f+n\omega}\right)^{1/2} J_n(\gamma_n)\mathrm{Ek}_n^{1/2}. \tag{B1}$$

Utilizing the definition of Ek_n, this can be rewritten as

$$E_{T_n} \sim \frac{f}{f+n\omega} J_n(\gamma_n)\mathrm{Ek}_0^{1/2}. \tag{B2}$$

Taking the limit of (B2) as $f + n\omega \rightarrow 0$ gives $|E_{T_n}| \sim \mathrm{Ek}_0^{1/2}/2$ if $n = \pm 1$ and $E_{T_n} \sim 0$ if $n = \pm 2$. Thus, because of the behavior of the Bessel functions as their argument goes to zero, the errors associated with these modes where the WKBJ approximation is formally invalid are at worst $O(\mathrm{Ek}_0^{1/2})$, and ensuring the validity of the WKBJ approximation for $n = 0$ remains sufficient to ensure validity for all modes.

REFERENCES

Balmforth, N. J., and R. V. Craster, 2001: Geophysical aspects of non-Newtonian fluid mechanics. *Geomorphological Fluid Mechanics*, N. J. Balmforth, and A. Provenzale, Eds., Lecture Notes in Physics, Vol. 582, Springer, 34–51, doi:10.1007/3-540-45670-8_2.

Bender, C. M., and S. A. Orszag, 1978: *Advanced Mathematical Methods for Scientists and Engineers.* McGraw-Hill, 593 pp.

Bernie, D. J., E. Guilyardi, G. Madec, J. M. Slingo, and S. J. Woolnough, 2007: Impact of resolving the diurnal cycle in an ocean–atmosphere GCM. Part 1: A diurnally forced OGCM. *Climate Dyn.*, **29**, 575–590, doi:10.1007/s00382-007-0249-6.

——, ——, ——, ——, ——, and J. Cole, 2008: Impact of resolving the diurnal cycle in an ocean–atmosphere GCM. Part 2: A diurnally coupled CGCM. *Climate Dyn.*, **31**, 909–925, doi:10.1007/s00382-008-0429-z.

Blackadar, A. K., 1957: Boundary layer wind maxima and their significance for the growth of nocturnal inversions. *Bull. Amer. Meteor. Soc.*, **38**, 283–290.

Brainerd, K. E., and M. C. Gregg, 1993: Diurnal restratification and turbulence in the oceanic surface mixed layer: 1. Observations. *J. Geophys. Res.*, **98**, 22 645–22 656, doi:10.1029/93JC02297.

Buajitti, K., and A. K. Blackadar, 1957: Theoretical studies of diurnal wind-structure variations in the planetary boundary layer. *Quart. J. Roy. Meteor. Soc.*, **83**, 486–500, doi:10.1002/qj.49708335804.

Cannon, J. R., 1984: *The One-Dimensional Heat Equation.* Encyclopedia of Mathematics and Its Applications, Vol. 23, Cambridge University Press, 483 pp.

Chen, S. S., and R. A. Houze, 1997: Diurnal variation and life-cycle of deep convective systems over the tropical Pacific warm pool. *Quart. J. Roy. Meteor. Soc.*, **123**, 357–388, doi:10.1002/qj.49712353806.

Clayson, C. A., and A. Chen, 2002: Sensitivity of a coupled single-column model in the tropics to treatment of the interfacial parameterizations. *J. Climate*, **15**, 1805–1831, doi:10.1175/1520-0442(2002)015<1805:SOACSC>2.0.CO;2.

Csanady, G. T., and P. T. Shaw, 1980: The evolution of a turbulent Ekman layer. *J. Geophys. Res.*, **85**, 1537–1547, doi:10.1029/JC085iC03p01537.

Dai, A., and K. E. Trenberth, 2004: The diurnal cycle and its depiction in the community climate system model. *J. Climate*, **17**, 930–951, doi:10.1175/1520-0442(2004)017<0930:TDCAID>2.0.CO;2.

Danabasoglu, G., W. G. Large, J. J. Tribbia, P. R. Gent, B. P. Briegleb, and J. C. McWilliams, 2006: Diurnal coupling in the tropical oceans of CCSM3. *J. Climate*, **19**, 2347–2365, doi:10.1175/JCLI3739.1.

Davis, R., R. de Szoeke, and P. Niiler, 1981: Variability in the upper ocean during MILE. Part II: Modeling the mixed layer response. *Deep-Sea Res.*, **28A**, 1453–1475, doi:10.1016/0198-0149(81)90092-3.

Elipot, S., and S. T. Gille, 2009: Ekman layers in the Southern Ocean: Spectral models and observations, vertical viscosity and boundary layer depth. *Ocean Sci.*, **5**, 115–139, doi:10.5194/os-5-115-2009.

Grisogono, B., 1995: A generalized Ekman layer profile with gradually varying eddy diffusivities. *Quart. J. Roy. Meteor. Soc.*, **121**, 445–453, doi:10.1002/qj.49712152211.

Huang, N. E., 1979: On surface drift currents in the ocean. *J. Fluid Mech.*, **91**, 191–208, doi:10.1017/S0022112079000112.

Jerlov, N. G., 1976: *Marine Optics.* Elsevier, 231 pp.

Kawai, Y., and A. Wada, 2007: Diurnal sea surface temperature variation and its impact on the atmosphere and ocean: A review. *J. Oceanogr.*, **63**, 721–744, doi:10.1007/s10872-007-0063-0.

Kim, S. Y., P. M. Kosro, and A. L. Kurapov, 2014: Evaluation of directly wind-coherent near-inertial surface currents off Oregon using a statistical parameterization and analytical and numerical models. *J. Geophys. Res. Oceans*, **119**, 6631–6654, doi:10.1002/2014JC010115.

Large, W. G., J. C. McWilliams, and S. C. Doney, 1994: Oceanic vertical mixing: A review and a model with a nonlocal boundary layer parameterization. *Rev. Geophys.*, **32**, 363–403, doi:10.1029/94RG01872.

Lenn, Y.-D., and T. K. Chereskin, 2009: Observations of Ekman currents in the Southern Ocean. *J. Phys. Oceanogr.*, **39**, 768–779, doi:10.1175/2008JPO3943.1.

Lewis, D., and S. Belcher, 2004: Time-dependent, coupled, Ekman boundary layer solutions incorporating Stokes drift. *Dyn. Atmos. Oceans*, **37**, 313–351, doi:10.1016/j.dynatmoce.2003.11.001.

Mangat, P. S., and B. T. Molloy, 1994: Prediction of long term chloride concentration in concrete. *Mater. Struct.*, **27**, 338–346, doi:10.1007/BF02473426.

Marshall, J., C. Hill, L. Perelman, and A. Adcroft, 1997: Hydrostatic, quasi-hydrostatic, and nonhydrostatic ocean modeling. *J. Geophys. Res.*, **102**, 5733–5752, doi:10.1029/96JC02776.

McCreary, J. P., K. E. Kohler, R. R. Hood, S. Smith, J. Kindle, A. S. Fischer, and R. A. Weller, 2001: Influences of diurnal and intraseasonal forcing on mixed-layer and biological variability in the central Arabian Sea. *J. Geophys. Res.*, **106**, 7139–7155, doi:10.1029/2000JC900156.

McWilliams, J. C., and E. Huckle, 2006: Ekman layer rectification. *J. Phys. Oceanogr.*, **36**, 1646–1659, doi:10.1175/JPO2912.1.

——, ——, and A. F. Shchepetkin, 2009: Buoyancy effects in a stratified Ekman layer. *J. Phys. Oceanogr.*, **39**, 2581–2599, doi:10.1175/2009JPO4130.1.

O'Brien, J. J., 1970: A note on the vertical structure of the eddy exchange coefficient in the planetary boundary layer. *J. Atmos. Sci.*, **27**, 1213–1215, doi:10.1175/1520-0469(1970)027<1213:ANOTVS>2.0.CO;2.

Price, J. F., and M. A. Sundermeyer, 1999: Stratified Ekman layers. *J. Geophys. Res.*, **104**, 20 467–20 494, doi:10.1029/1999JC900164.

——, R. A. Weller, and R. Pinkel, 1986: Diurnal cycling: Observations and models of the upper ocean response to diurnal heating, cooling, and wind mixing. *J. Geophys. Res.*, **91**, 8411–8427, doi:10.1029/JC091iC07p08411.

Rascle, N., and F. Ardhuin, 2009: Drift and mixing under the ocean surface revisited: Stratified conditions and model-data comparisons. *J. Geophys. Res.*, **114**, C02016, doi:10.1029/2007JC004466.

Sheih, C. M., 1972: A theoretical study of the diurnal wind variations in the planetary boundary layer. *J. Atmos. Sci.*, **29**, 995–998, doi:10.1175/1520-0469(1972)029<0995:ATSOTD>2.0.CO;2.

Shinoda, T., 2005: Impact of the diurnal cycle of solar radiation on intraseasonal SST variability in the western equatorial Pacific. *J. Climate*, **18**, 2628–2636, doi:10.1175/JCLI3432.1.

Singh, M. P., R. T. McNider, and J. T. Lin, 1993: An analytical study of diurnal wind-structure variations in the boundary layer and the low-level nocturnal jet. *Bound.-Layer Meteor.*, **63**, 397–423, doi:10.1007/BF00705360.

Skeel, R. D., and M. Berzins, 1990: A method for the spatial discretization of parabolic equations in one space variable. *SIAM J. Sci. Stat. Comput.*, **11**, 1–32, doi:10.1137/0911001.

Smyth, W., 1854: *The Mediterranean: A Memoir, Physical, Historical and Nautical.* J. W. Parker and Son, 519 pp.

Smyth, W. D., J. N. Moum, L. Li, and S. A. Thorpe, 2013: Diurnal shear instability, the descent of the surface shear layer, and the deep cycle of equatorial turbulence. *J. Phys. Oceanogr.*, **43**, 2432–2455, doi:10.1175/JPO-D-13-089.1.

Stommel, H., K. Saunders, W. Simmons, and J. Cooper, 1969: Observations of the diurnal thermocline. *Deep-Sea Res.*, **16** (Suppl.), 269–284.

Tan, Z.-M., and M. M. Farahani, 1998: An analytical study of the diurnal variations of wind in a semi-geostrophic Ekman boundary layer model. *Bound.-Layer Meteor.*, **86**, 313–332, doi:10.1023/A:1000694732459.

Temme, N. M., 1996: *Special Functions: An Introduction to the Classical Functions of Mathematical Physics.* Wiley, 374 pp.

Vallis, G. K., 2006: *Atmospheric and Oceanic Fluid Dynamics: Fundamentals and Large-Scale Circulation.* Cambridge University Press, 745 pp.

Van de Wiel, B. J. H., A. F. Moene, G. J. Steeneveld, P. Baas, F. C. Bosveld, and A. A. M. Holtslag, 2010: A conceptual view on inertial oscillations and nocturnal low-level jets. *J. Atmos. Sci.*, **67**, 2679–2689, doi:10.1175/2010JAS3289.1.

Weller, R. A., and A. J. Plueddemann, 1996: Observations of the vertical structure of the oceanic boundary layer. *J. Geophys. Res.*, **101**, 8789–8806, doi:10.1029/96JC00206.

Wenegrat, J. O., 2016: Ocean boundary layer dynamics and air-sea interaction. Ph.D. Thesis, University of Washington, Seattle, 168 pp. [Available online at http://hdl.handle.net/1773/35286.]

——, and M. J. McPhaden, 2015: Dynamics of the surface layer diurnal cycle in the equatorial Atlantic Ocean (0°, 23°W). *J. Geophys. Res. Oceans*, **120**, 563–581, doi:10.1002/2014JC010504.

——, and ——, 2016: Wind, waves, and fronts: Frictional effects in a generalized Ekman model. *J. Phys. Oceanogr.*, **46**, 371–394, doi:10.1175/JPO-D-15-0162.1.

——, ——, and R.-C. Lien, 2014: Wind stress and near-surface shear in the equatorial Atlantic Ocean. *Geophys. Res. Lett.*, **41**, 1226–1231, doi:10.1002/2013GL059149.

Zhang, Y., and Z.-M. Tan, 2002: The diurnal wind variation in a variable eddy viscosity semi-geostrophic Ekman boundary-layer model: Analytical study. *Meteor. Atmos. Phys.*, **81**, 207–217, doi:10.1007/s00703-001-0542-6.

Zikanov, O., D. N. Slinn, and M. R. Dhanak, 2003: Large-eddy simulations of the wind-induced turbulent Ekman layer. *J. Fluid Mech.*, **495**, 343–368, doi:10.1017/S0022112003006244.